Supplementary information

Electron rich triazine based covalent organic framework as aqueous electrolyte symmetric supercapacitor

Divya[1], Ravi Rajan Panday[2], Shahjad Ali[3], Md Ehesan Ali[3], Sarita Kalla[1], Rakesh K Pandey[2*], Ritambhara Jangir[1*]
[1]Sardar Vallabhbhai National Institute of Technology, Ichchanath, Surat-395 007, Gujarat, India.
[2]Department of Chemistry, Mahatma Gandhi Central University, East-Champaran, Motihari 845401, Bihar, India.
[3]Institute of Nano Science and Technology, Sector-81, Mohali, Punjab 140306, India.
*Corresponding Author: ritambhara.jangir@chem.svnit.ac.in

Instruments and Analytical Techniques

FT-IR spectra were obtained using a SHIMADZU IR Affinity-1 spectrometer, collecting 45 scans at a resolution of 4 cm^{-1}.

NMR spectra were obtained using a Jeol JNM-60090 R5S1 spectrometer at SAIF, IIT Patna, using DMSO-d_6 as the solvent and tetramethylsilane (TMS) as the external standard. Chemical shifts are reported in ppm.

HRMS analysis was performed at IIT Jammu using a Xevo G2-XS QToF 4k (LC-MS/MS) system, coupled with an Acquity H-Class PLUS UPLC system, achieving an m/z resolution of 100,000.

Solid-state NMR spectra were recorded at IISC Bangalore using a JEOL 400 MHz (ECX400) spectrometer equipped with a Bruker magic-angle-spinning (MAS) probe, accumulating 32,000 scans.

Powder XRD measurements were conducted using a Panalytical X'Pert Pro diffractometer. Data analysis was carried out using the Reflex module of Materials Studio V6.

Thermal stability was assessed using a TA Module Q600 thermogravimetric differential thermal analyzer (TGA-DTA). Samples were analyzed under a nitrogen gas flow (100 mL/min), heated from room temperature to 800 °C at a ramp rate of 10 K/min.

BET surface area and porosity of 200 mg samples was determined using a Nova Touch LX2 gas sorption analyzer (Quantachrome). Nitrogen adsorption isotherms were recorded at 77 K using ultrahigh-purity N_2 up to approximately 1 atm.

Morphological analysis was performed using a Nova Nano FE-SEM 450 (FEI) scanning electron microscope. Prior to imaging, samples were coated with a platinum (Pt) layer via sputtering for 100 s.

TEM images were obtained using a Tecnai G2 20 S-TWIN (FEI) microscope operating at an accelerating voltage of 200 kV. Diffraction patterns were recorded at a scanning rate of 1° min^{-1} over a 20°–80° range.

XPS analysis was conducted using a Thermo Fisher Nexsa instrument with a monochromatic Al Kα X-ray source under ultra-high vacuum (base pressure: 10^{-8} mbar). Survey scans were acquired at a pass energy of 200 eV with a dwell time of 10 ms per data point. The binding energy scale was calibrated between 0 and 1350 eV, referencing the C 1s peak at 284.8 eV.

An electron flood gun was used for charge compensation to prevent charge buildup on insulating samples.

The zeta potential of a 1 mg/mL COF suspension in distilled water was measured using a HORIBA Scientific Nano Particle Analyzer SZ-100V2.

Density functional theory (DFT), as implemented in the SIESTA program, was used to examine the structural and electrical characteristics of TDMTA-TFP-COF.43Troullier-Martins norm-conserving pseudopotentials were used to explain the core-valence interactions, whereas the double-ζ polarization basis set (DZP) was used to describe the valence electrons.[1, 2] The Perdew–Burke–Ernzerhof (PBE) representation of the generalized gradient approximation (GGA) was used to approximate the exchange-correlation functional.46 The geometry is optimized using the conjugate gradient approach until the atomic forces converge to 0.01 eVÅ-1. For electronic structure calculations, a 6×6×6 Monkhorst-Pack k-grid with a mesh cutoff of 400 Ry was employed. The long-range interactions are treated using Grimme's three-body correction (D3).[3]

Electrochemical measurements were performed using a Squidstat Plus potentiostat (Admiral Instruments, USA). Cyclic voltammetry (CV) and galvanostatic charge-discharge (GCD) tests were conducted over three cycles, with the third cycle used for data analysis. For capacitance retention studies, the first CV cycle was disregarded.[4]

Chemicals: 4-Amino-3,5-dimethylbenzonitrile was purchased from BLD Pharma. Dichloromethane, mesitylene, dioxane, methanol, DMF, acetone, NMP, and acetic acid were purchased from Spectrochem. Trifluoromethanesulfonic acid (triflic acid) was obtained from Sigma-Aldrich. NaOH and KCl were purchased from SRL. Super P (carbon black), PVDF (polyvinylidene difluoride), and 0.5 mm graphite sheets were procured from a local vendor.

Synthesis of 4,4',4''-(1,3,5-triazine-2,4,6-triyl)tris(2,6-dimethylaniline) (TDMTA):

4-Amino-3,5-dimethylbenzonitrile (1.45 g) was dissolved in 40 mL of dichloromethane. Subsequently, 2.5 mL of triflic acid was added dropwise to the flask under an inert atmosphere at room temperature. The resulting solution was stirred overnight under nitrogen at 100°C. After the reaction, 200 mL of distilled water was added to the solution to facilitate dilution, and the acidic nature was neutralized using a 2 M NaOH solution. The resulting deep yellow precipitate was washed thoroughly with water several times to remove impurities. Finally, the product was dried under vacuum, yielding the desired compound.[5] The obtained precursor TDMTA was dissolved in a 1:1 (v/v) methanol and DMF solution to grow its crystals. The concentration of the solution was 10 mg/mL to grow crystals of TDMTA. ^{1}H NMR (500 MHz,) δ 8.3 (s)for six aromatic protons, 3.95 (s) for six protons attached to ammine group, 2.34 (s) for eighteen protons of methyl group.

Synthesis of TDMTA-TFP-COF:

To synthesize the novel imine-based COF, equimolar amounts (0.1 mmol) of C_3-symmetric monomers, TFP (triformyl phloroglucinol) and TDMTA (4,4',4''-(1,3,5-triazine-2,4,6-triyl)tris(2,6-dimethylaniline)) were used. A mixture of TFP and TDMTA was prepared in 6 mL of mesitylene and dioxane (1:1, v/v).

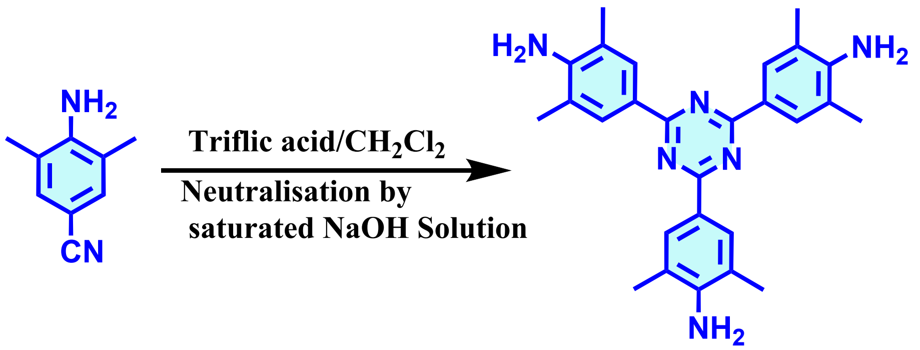

Figure S1: synthesis of 4,4',4''-(1,3,5-triazine-2,4,6-triyl)tris(2,6-dimethylaniline) (TDMTA).

This mixture was sonicated until it becomes a homogeneous solution. Subsequently, this solution was transferred into a glass ampule using a syringe. To acidify the reaction, 0.6 mL of 6 M acetic acid was added. The glass ampule was frozen, degassed, and filled with N2 gas to ensure an optimal nitrogen atmosphere within the reaction system. Following the solvothermal method of COF preparation, the sealed ampule was placed in a programmable oven at 120°C and maintained at the same temperature for 5 days to facilitate the polymerization process. A cooling rate of 0.1875 °C min-1 was maintained after 5 days of heating. Upon reaching the room temperature, the ampule was carefully broken to obtain the reaction product, which was then filtered and thoroughly washed with organic solvents, including methanol, acetone, dioxane, and DMF, to remove any impurities. The resultant yellow product was dried at 100 °C for 12 hours. The yield of the TDMTA-TFP-COF was quantified at 89%, and the product was subsequently characterized to confirm its structure and properties.

In Figure S2, the reversible arrow (⇌) signifies the dynamic covalent nature of imine bond formation in the synthesis of imine-linked covalent organic frameworks (COFs). This process involves a condensation reaction between an amine (-NH_2) and an aldehyde (-CHO), yielding an imine (-C=N-) and water as a byproduct. The reversibility of this reaction is crucial, as under specific conditions — such as in the presence of water, acids, or heat — the imine bond can break, regenerating the amine and aldehyde.

This dynamic reversibility plays a pivotal role in COF synthesis by enabling error correction and self-healing during framework formation. Defective or misaligned bonds can break and reform, driving the system toward a more stable and highly ordered crystalline structure. This process enhances both the structural integrity and overall crystallinity of the COF, ensuring the formation of well-ordered frameworks.[6, 7]

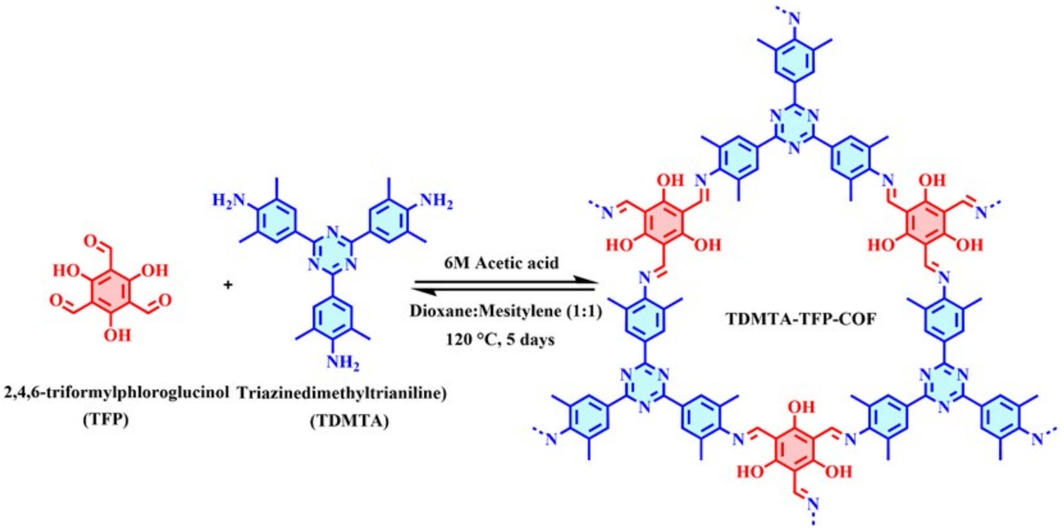

Figure S2: Synthesis scheme for TDMTA-TFP-COF from its precursors.

Electrode Preparation:

For Three Electrode System: Because the TDMTA-TFP COF is not stitched with working electrode support, so we mixed 8 mg of synthesized COF powder, 1 mg of poly(vinylidene difluoride) (PVDF) binder, and 1 mg of super-p in 1 mL of N-methyl-2-pyrrolidone (NMP) solvent for a three-electrode setup. The COF slurry is applied onto a 0.5 mm graphite sheet (1 cm × 1 cm) as a working electrode for a three-electrode setup. We deposited ~0.7 mg of COF onto the electrode. The working electrode was dried overnight at room temperature (~25°C).

For the symmetrical supercapacitor: Unlike the three-electrode system, we do not use binders in electrode preparation because the main drawback of this approach is the Pore obstruction caused by them. These can reduce the accessibility of active sites within COFs for substrates and charge carriers.[8, 9] So, to address the issue mentioned above, construct the electrodes without the use of a binders. To prepare negative and positive electrodes, 8 mg of TDMTA-TFP COF dissolved in 1 mL of NMP solvent. The COF slurry is applied onto a 0.5 mm graphite sheet (1 cm × 1 cm) as both negative and positive electrodes. The working electrode was dried overnight at 80°C and then left at room temperature (~25°C) for an additional overnight period. Regarding the evaporation of NMP at 80°C, while its boiling point is around 202°C, its evaporation is still feasible at lower temperatures due to its vapor pressure and volatility. Several factors facilitate NMP removal under these conditions, e.g., at 80°C, NMP has a significantly higher vapor pressure than at room temperature, enhancing its evaporation. Although it does not reach its boiling point, the solvent gradually evaporates over time. In addition, if dried in a ventilated oven or under vacuum, the continuous removal of evaporated NMP enhances its elimination. While a significant portion of NMP evaporates at 80°C overnight (~12-16 hours), some residual solvent may still be present. The additional overnight drying at room temperature (~25°C) ensures further solvent removal.

Supercapacitor Fabrication:

We prepared a sandwich-type device with fabricated electrodes (positive and negative) separated by an NKK membrane that was soaked thoroughly 1 M KCl electrolyte, and Ni wire was used for the connection. We deposited ~2 mg of the COF onto the electrode. During the experiments, 50 cycles of CV at 100 mV/s are conducted in both three-electrode and symmetric cell setups to achieve stability before recording data.

Calculation:

For both three electrode and two electrode setups, the specific capacitance (C_s) computed from the CV curves using following formula[10, 11]:

$$C_s\left(\frac{F}{g}\right) = \frac{\int_{E_i}^{E_f} i(E)d(E)}{\eta\left(E_f - E_i\right)m}$$

Where, E_i and E_f are initial potential (V) and final potential (V) respectively. $\int_{E_i}^{E_f} i(E)d(E)$ is total charge (area) under the CV curve. η and m are scan rate (V/s) and mass of electrode (g) respectively.

The specific capacitance (C_s) calculated from the discharging curves of GCD For both three electrode SCs according to the following formula[10]:

$$C_s\left(\frac{F}{g}\right) = \frac{i\Delta t}{(E_f - E_i)m}$$

Where, E_i, E_f, Δt and m are initial potential (V), final potential respectively (V), time in seconds for discharging and m is the mass in grams.

For SCs (two electrode setup) energy density (E_d) calculated from the GCD in accordance with the following formula[12, 13]:

$$E_d\left(\frac{Wh}{g}\right) = \frac{Cs \times (dV)^2}{7200}$$

Where, dV is the potential window, after eliminating the impact of the iR drop, the potential window dV is taken from the GCD curves.

The power density (P_d) for SCs computed from the GCD using following formula[12, 14]:

$$P_d\left(\frac{W}{g}\right) = \frac{E_d}{\Delta t} \times 3600$$

And Rser for SCs computed from the GCD using the following equation:

$$Rser = \frac{V_{drop}}{2i}$$

Where, i is current.

Figure S7 displays the UV–vis spectra of COF, demonstrating a wide absorption in visible region, reaching up to 550 nm. The absorption band beyond 520 nm is associated with efficient intramolecular charge transfer, an extensively conjugated network, strong π–π interactions, and high crystallinity. The optical band gap, estimated using the Tauc plot, was determined to be 2.34 eV.[15]

Tauc presented a method in 1966 for using optical absorption spectra to calculate the band gap energy of amorphous semiconductors. His concept was later expanded upon by Davis and Mott. The Tauc method operates on the assumption that the absorption coefficient α varies with energy and can be represented by the following equation.

$$(\alpha \cdot h\nu)^{\left(\frac{1}{\gamma}\right)} = B(h\nu - Eg)$$

In this case, h stands for Planck's constant, ν for photon frequency, Eg for band gap energy, and B for constant. The value of the factor γ, which is 1/2 for direct band gaps and 2 for indirect band gaps, varies according to the kind of electron transition.[16]

Zeta potential of TDMTA-TFP COF was calculated to find the surface charge of the material. From zeta it is concluded that material is having surface charge of – 39mV (Figure S11).

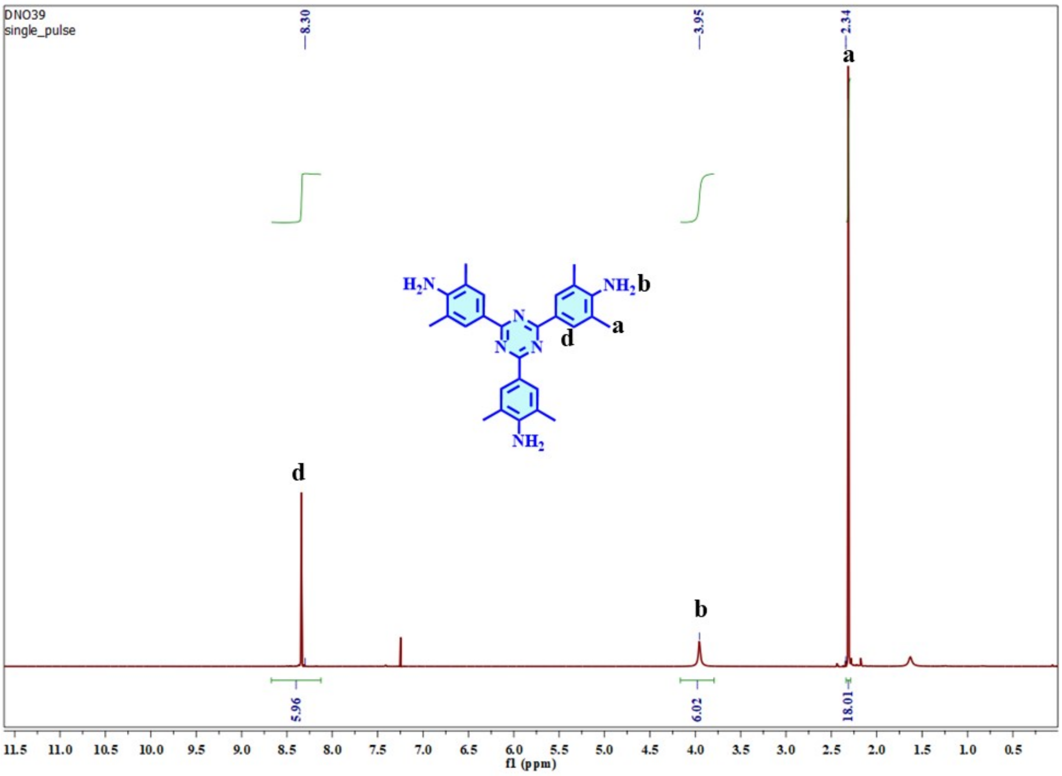

Figure S3: ^{1}H NMR of 4,4',4''-(1,3,5-triazine-2,4,6-triyl)tris(2,6-dimethylaniline) (TDMTA).

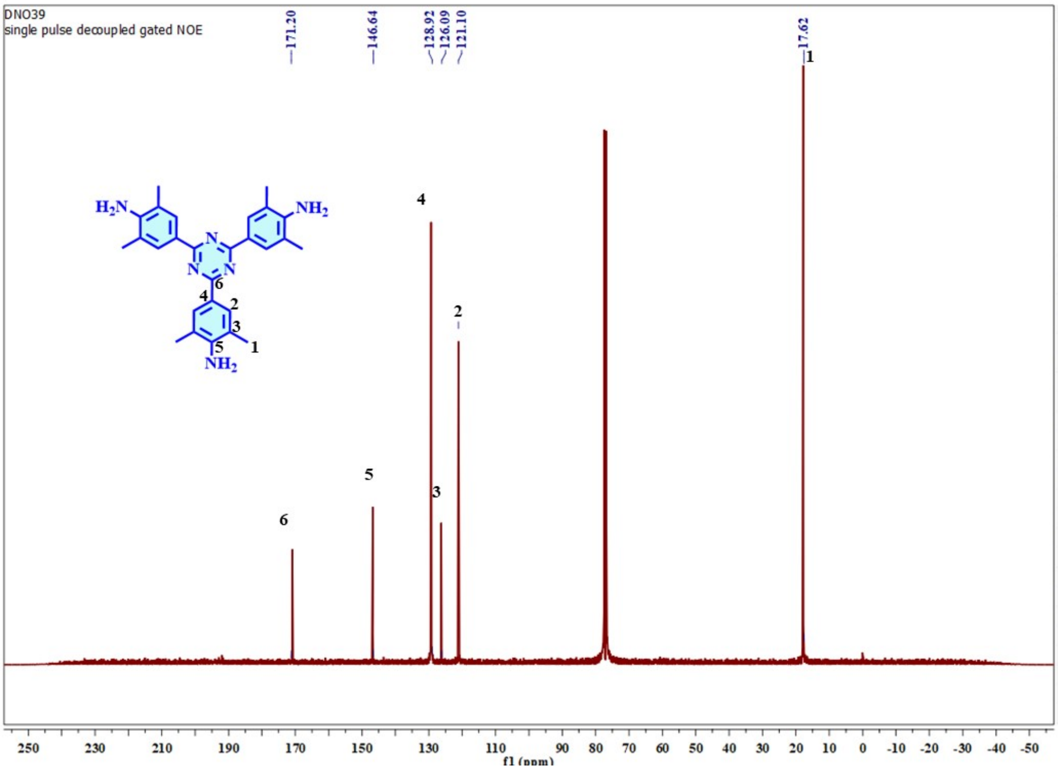

Figure S4: ^{13}C NMR spectrum of 4,4',4''-(1,3,5-triazine-2,4,6-triyl)tris(2,6-dimethylaniline) (TDMTA).

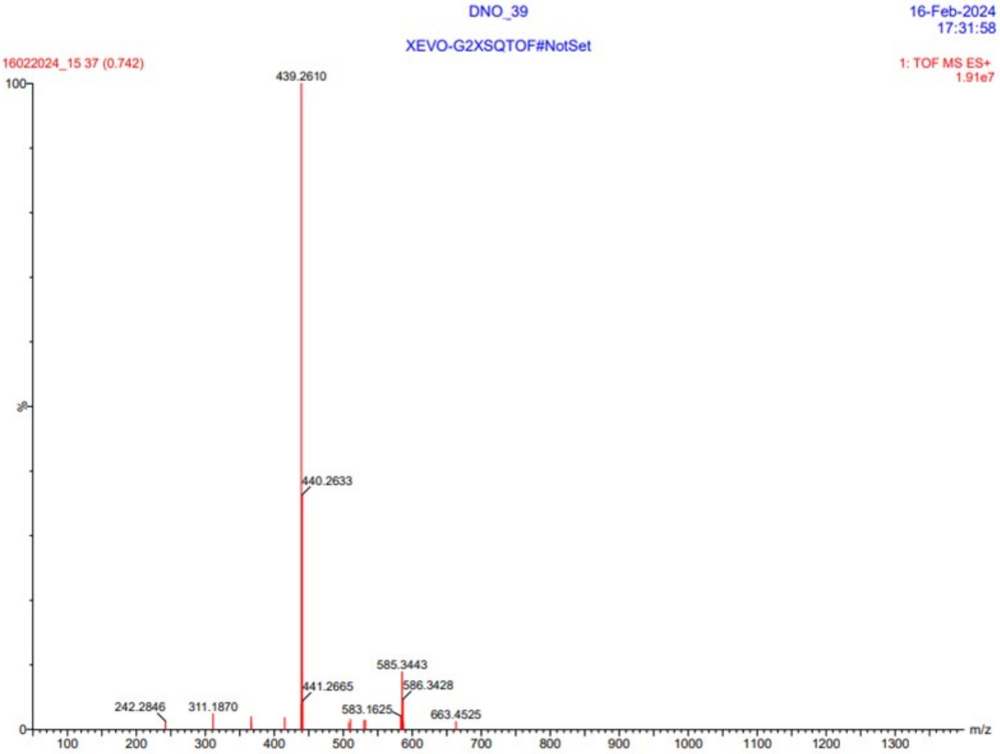

Figure S5: HRMS of precursor 4,4',4''-(1,3,5-triazine-2,4,6-triyl)tris(2,6-dimethylaniline) (TDMTA).

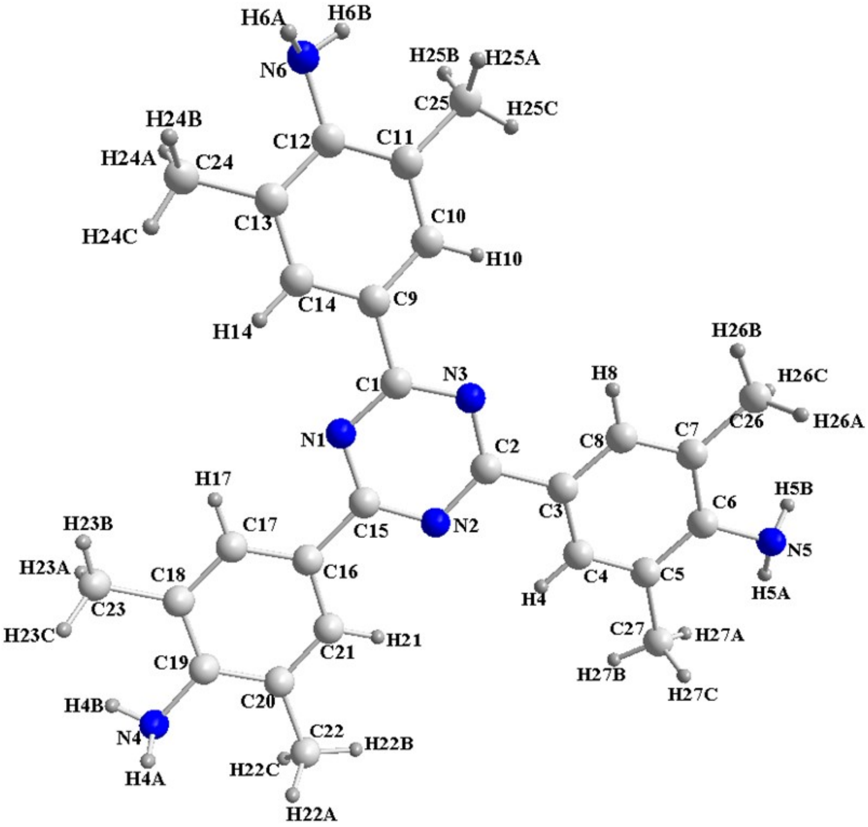

Figure S6: Crystal structure of precursor TDMTA.

Table S1: Crystal data and structure refinement for TDMTA.

CCDC deposition number	2427795
Empirical formula	$C_{27}H_{30}N_6$
Formula weight	438.57
Temperature/K	286.0
Crystal system	orthorhombic
Space group	$Pca2_1$
a/Å	14.350(2)
b/Å	13.941(2)
c/Å	23.623(4)
α/°	90
β/°	90
γ/°	90
Volume/Å^3	4726.0(13)

Z	8
ρ_{calc}g/cm^3	1.233
μ/mm^{-1}	0.076
F(000)	1872.0
Crystal size/mm^3	0.24 × 0.17 × 0.12
Radiation	MoKα (λ = 0.71073)
2Θ range for data collection/°	2.922 to 50.698
Index ranges	$-17 \le h \le 17$, $-16 \le k \le 16$, $-27 \le l \le 28$
Reflections collected	41251
Independent reflections	8570 [R_{int} = 0.0585, R_{sigma} = 0.0847]
Data/restraints/parameters	8570/1/613
Goodness-of-fit on F^2	1.028
Final R indexes [I>=2σ (I)]	R_1 = 0.0574, wR_2 = 0.1370
Final R indexes [all data]	R_1 = 0.0877, wR_2 = 0.1542
Largest diff. peak/hole / e Å^{-3}	0.23/-0.26
Flack parameter	-1.1(10)

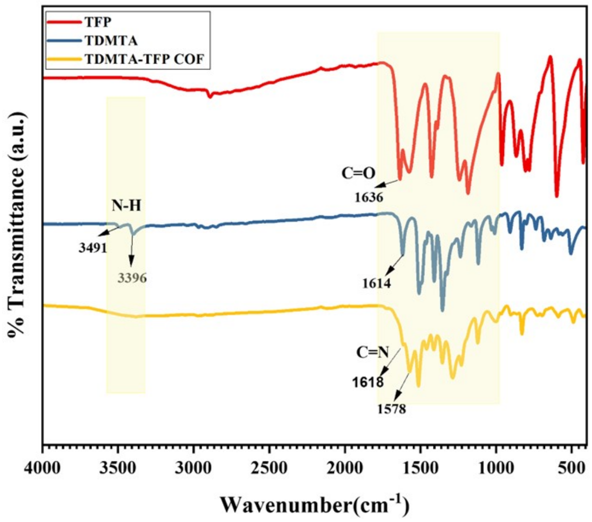

Figure S7: Comparative FTIR spectra of TDMTA-TFP-COF with monomers.

Formula:	C	H	N	O

$C_{36}H_{30}N_6O_3$				
Calculated	72.71	5.09	14.13	8.07
Experimental	61.58	5.179	11.78	-

Table S2: CHN analysis for TDMTA-TFP COF.

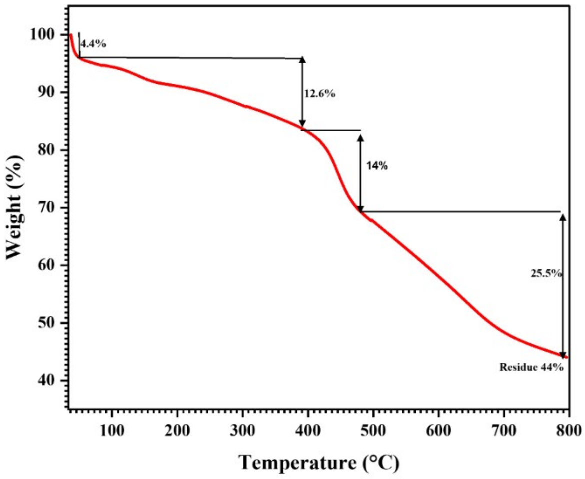

Figure S8: TGA plot for TDMTA-TFP COF.

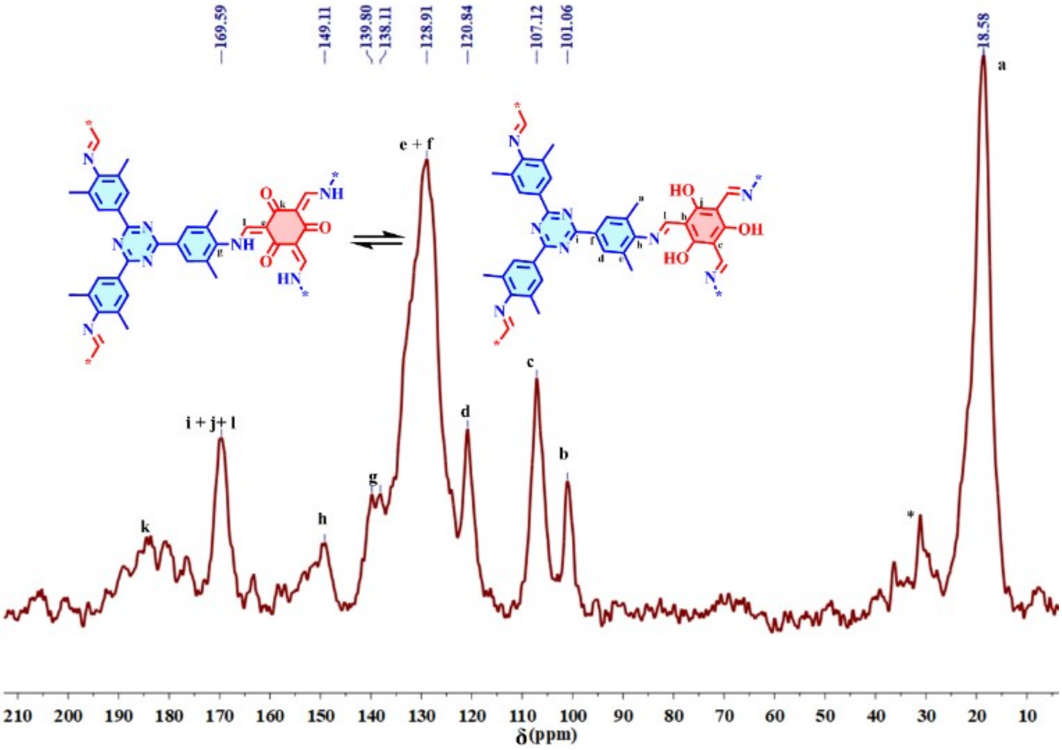

Figure S9: CP-MAS 13C NMR of TDMTA-TFP-COF (10 KHz, 300 K).

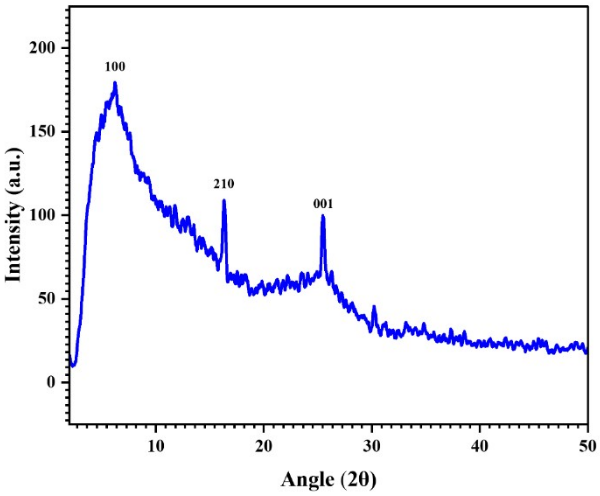

Figure S10: Powder X -ray diffraction of TDMTA-TFP-COF.

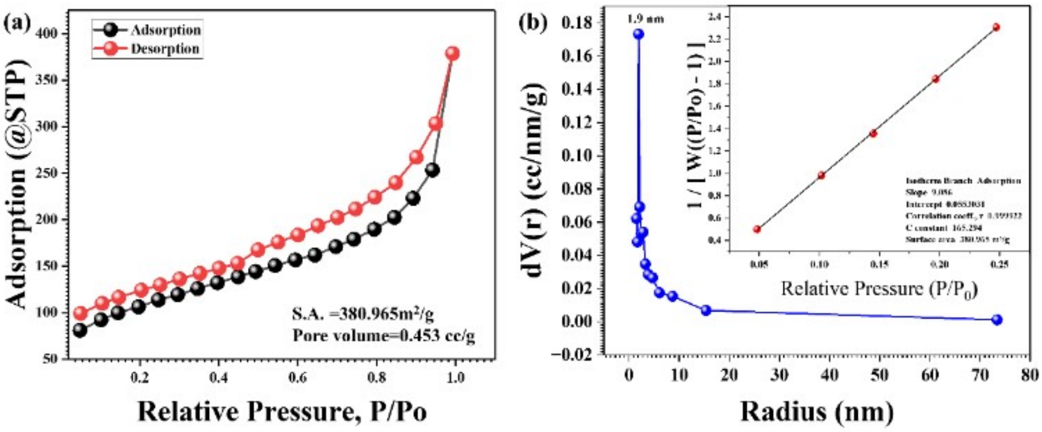

Figure S11: (a) N_2 adsorption/desorption profile, and (b) BET isotherm and Pore distribution of TDMTA-TFP-COF at a bath temperature of 77.35 K.

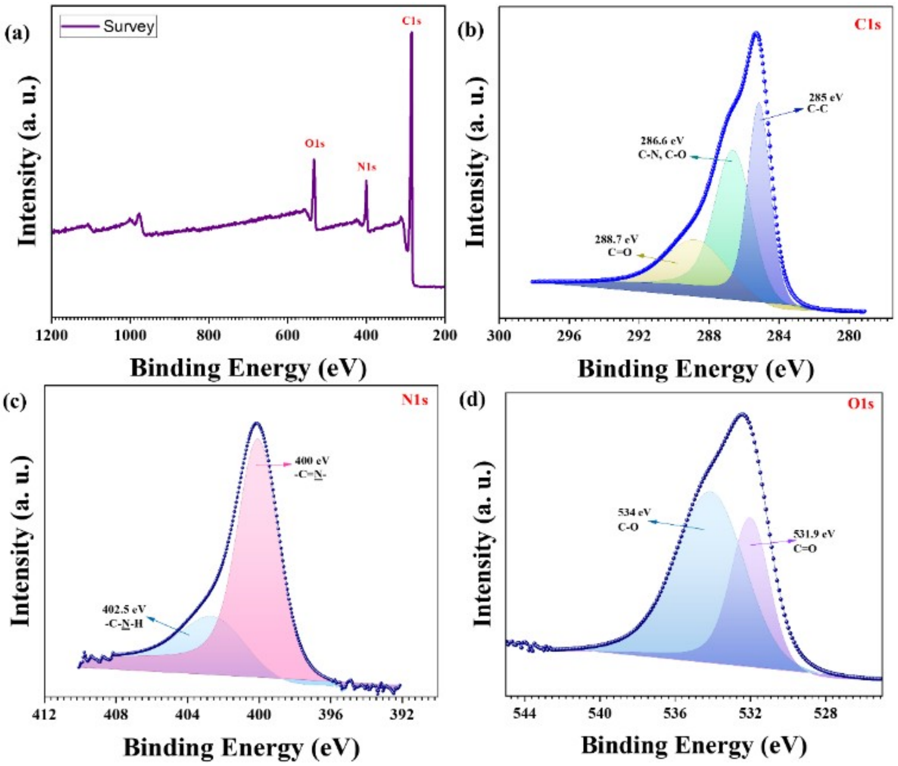

Figure S12: The typical XPS survey spectra (a), and high-resolution XPS spectra of C 1s (b), N1s (c), and O 1s (d).

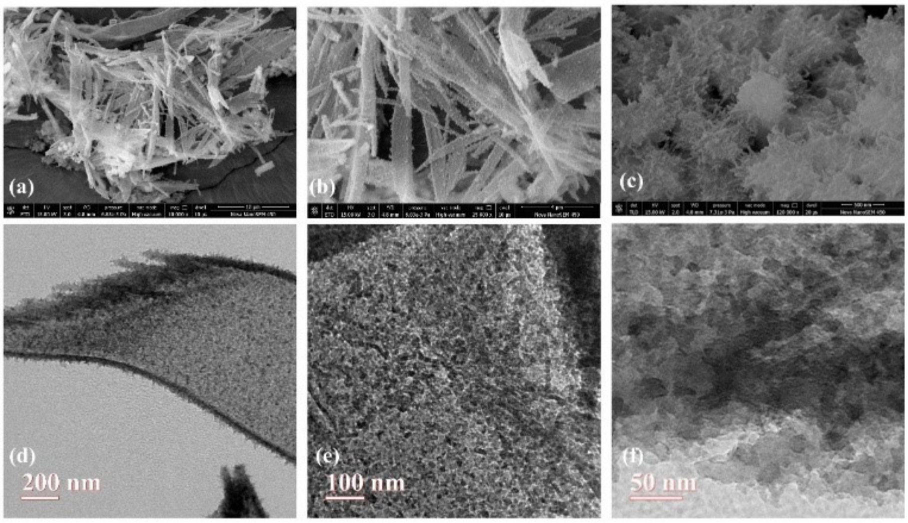

Figure S13: SEM images (a: 10 µm, b: 4 µm, and c: 500 nm) and TEM images (d: 200 nm, e: 100 nm, and f: 50 nm) of TDMTA-TFP-COF.

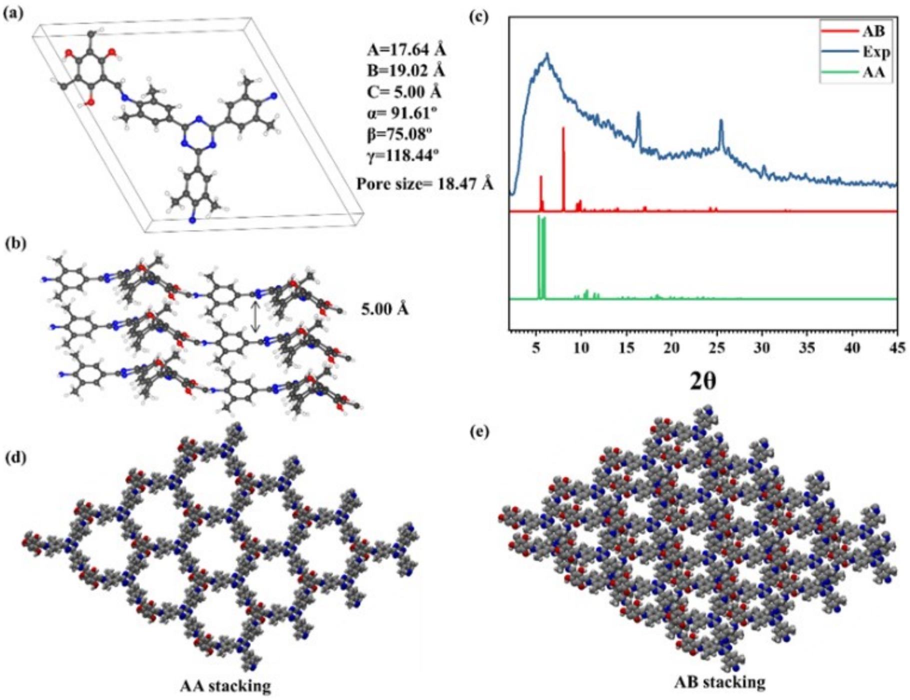

Figure S14: (a) The smallest unit cell of TDMTA-TFP-COF, (b) interlayer distance in the COF structure, (c) experimental PXRD pattern alongside PXRD simulations for AA and AB stacking, (d) 6×6×6 supercell of AA stacking illustrating pore size, and (e) 6×6×6 supercell of AB stacking. Colour codes: Carbon (grey), Hydrogen (white), Nitrogen (blue), and Oxygen (red).

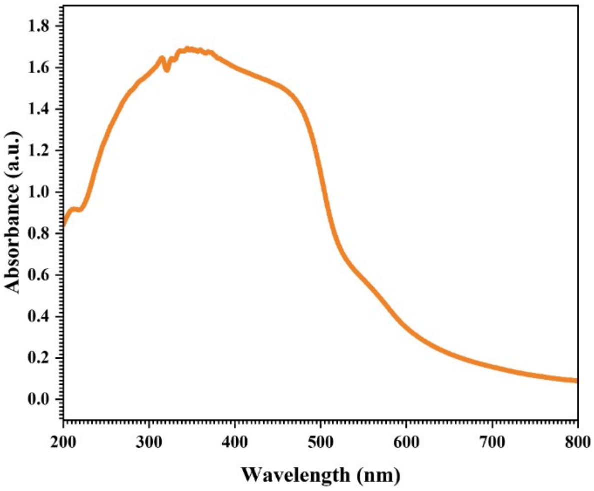

Figure S15: Solid state UV-Vis spectra of TDMTA-TFP COF.

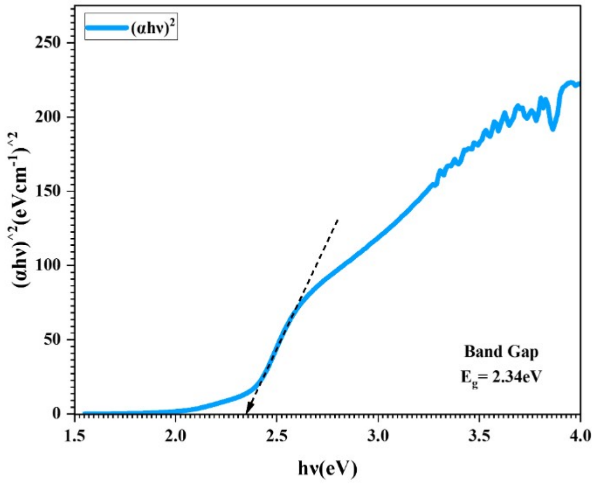

Figure S16: Tauc plot for optical band gap of TDMTA-TFP COF.

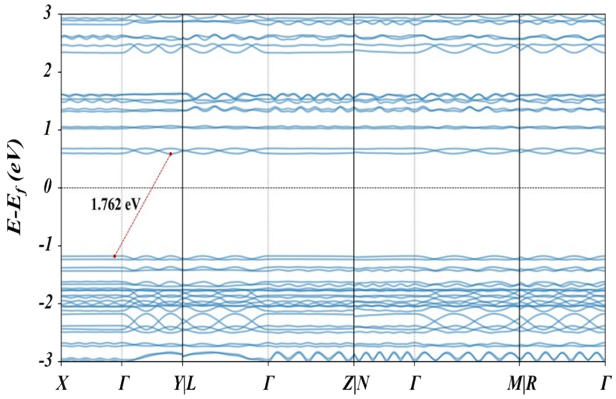

Figure S17: The indirect band structure of TDMTA-TFP COF in AA stacking, as calculated using DFT.

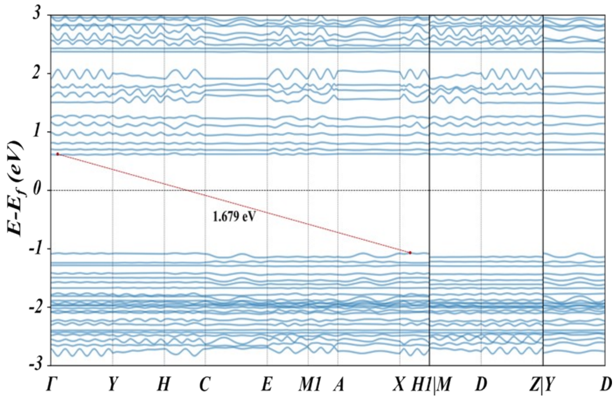

Figure S18: The indirect band structure of TDMTA-TFP COF in AB stacking, as calculated using DFT.

The difference between the theoretical and experimental bandgap values in covalent organic frameworks (COFs) can be attributed to several factors. Theoretical calculations typically consider an ideal, defect-free structure in a vacuum or periodic boundary conditions, which may not fully capture real-world conditions. In contrast, experimental measurements are influenced by factors such as structural defects, impurities, interlayer interactions, and environmental effects like solvent molecules or surface adsorbates.[17]

Additionally, theoretical methods often employ approximations (e.g., DFT with specific functionals) that can underestimate or overestimate the bandgap. Experimental techniques, such as UV-Vis or electrochemical methods, may also introduce measurement-related discrepancies. These combined effects contribute to the observed differences between theoretical predictions and experimental results.

Stacking interactions in covalent organic frameworks (COFs) significantly influence their electronic properties by modulating charge transport, band structure, and optical behavior. π–π stacking between adjacent layers facilitates charge delocalization and enhances conductivity by creating efficient pathways for electron hopping. However, variations in stacking modes (eclipsed vs. staggered) can lead to differences in orbital overlap, affecting the bandgap and charge mobility. Stronger stacking interactions generally reduce the bandgap by increasing electronic coupling, whereas disorder or misalignment can introduce localized states, leading to charge trapping and reduced conductivity.[18]

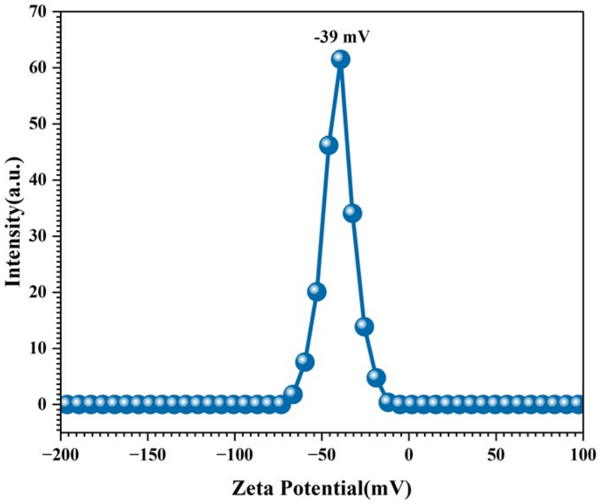

Figure S19: Zeta potential Vs Intensity Curve for TDMTA-TFP COF.

The electrochemical storage mechanism in the COF-based symmetric supercapacitor is governed by a combination of electric double-layer capacitance (EDLC) and pseudocapacitance. The OH and imine functional groups undergo tautomerization, facilitating proton-coupled electron transfer, while the triazine moiety contributes to reversible redox processes. Additionally, the high surface area and porous structure of the COF promote ion adsorption at the electrode/electrolyte interface, enhancing EDLC contributions. This dual mechanism is supported by the presence of redox peaks in the cyclic voltammetry (figure S20b) and non-linear characteristics in the charge-discharge profiles(figureS20e).

To quantitatively evaluate the charge storage mechanism and distinguish between capacitive and diffusion-controlled contributions in the studied electrode material, the Dunn method was employed.[19] The b values calculated with the help of modified power law $\log(i) = \log(a) + \log(b)$based of CV curves. The fitted slop b values were 0.67, reviling the hybrid charge storage process. This analysis utilizes the relationship, $I = k_1 * v + k_2 * v^{0.5}$

where $k_1 * v$ corresponds to the capacitive contribution and $k_2 * v$ to the diffusion-controlled part.

The capacitive and diffusive contributions were systematically calculated at scan rates ranging from 5 to 1000 mV s^{-1}.

As detailed in Figure S20 (l), a clear trend emerged wherein the capacitive contribution increased from ~20.7% at 5 mV s^{-1} to ~78.7% at 1000 mV s^{-1}, while the diffusion-controlled share declined correspondingly. This indicates that at higher scan rates, the current response becomes increasingly dominated by surface-controlled (capacitive) processes due to faster ion transport limitations in the bulk.

A representative CV curve recorded at 100 mV s^{-1} is shown in Figure S20(k), highlighting the hybrid nature of the charge storage. The Dunn analysis revealed that at this scan rate, the capacitive contribution reached ~53.8%, and the remaining ~46.2% originated from diffusion-controlled mechanisms. This near-equal distribution emphasizes the material’s synergistic pseudocapacitive and battery-type characteristics.

The increase in capacitive dominance with scan rate strongly suggests an accessible surface area and fast surface redox behaviour, aligning with the intended design of high-rate energy storage materials. Such behaviour is particularly beneficial in supercapacitor or hybrid capacitor applications requiring rapid charge–discharge cycles without significant performance loss.

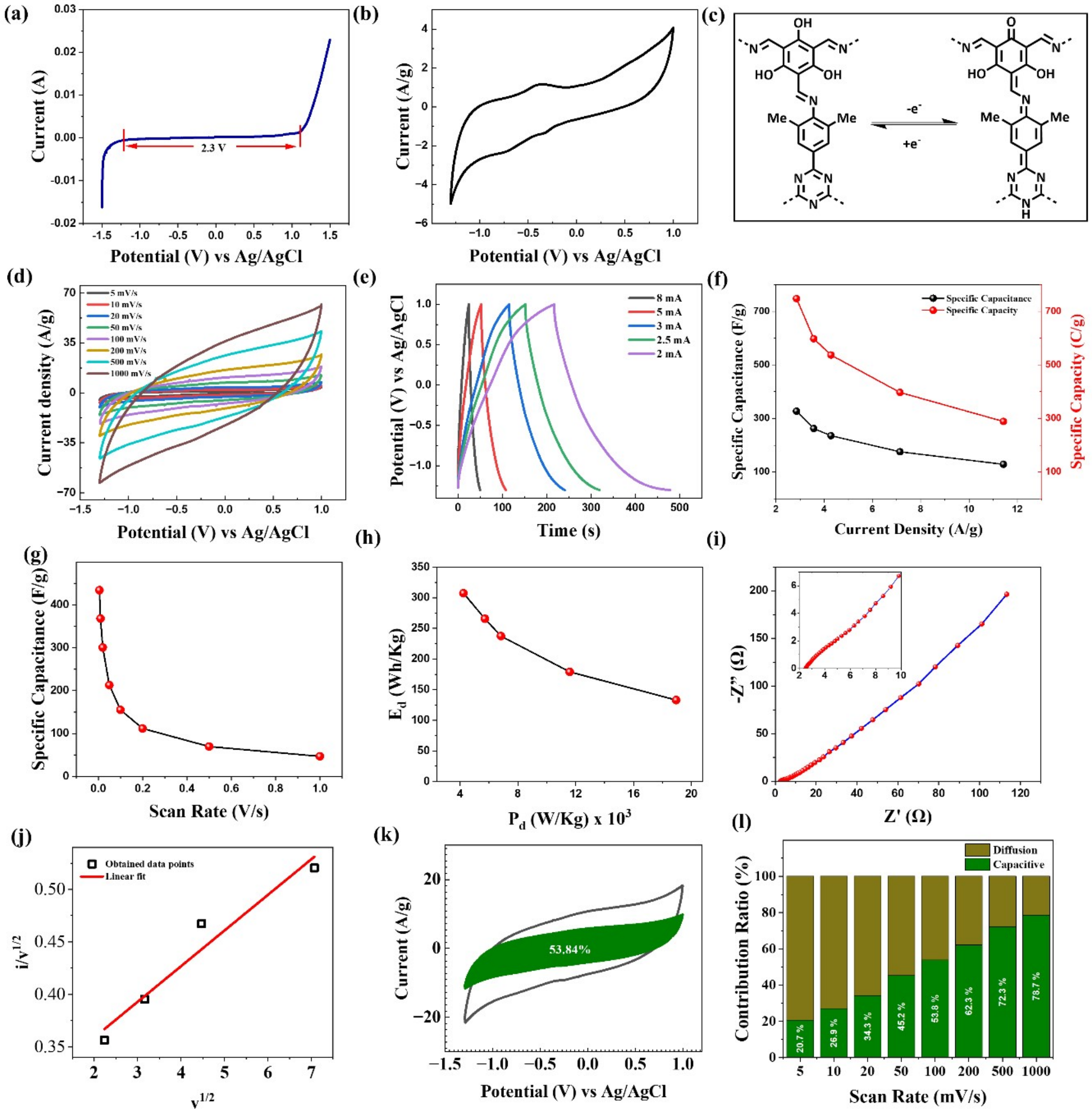

Figure S20: Electrochemical performance of TDMTA-TFP-COF in 1M KCl electrolyte in three-electrodes configuration: (a) Long-range LSV measurement at 5 mV/s. (b) CV curve measured at 5 mV/s (c) Possible redox behaviour taking place during the electrochemical process. (d) CV curves at different scan rates. (e) GCD curves measured at different currents. (f) Specific capacitance (F/g) (black) and specific capacity (C/g) (red) at different current densities. (g) Specific capacitance (F/g) at different scan rates. (h) Power Density (Pd) vs Energy Density (Ed) graph at different current densities. (i) Nyquist plot (j)$\frac{i}{v^{\frac{1}{2}}}$ vs $v^{\frac{1}{2}}$plot (k) CV curve recorded at 100 mV s^{-1} (l) Capacitive contributions of TDMTA-TFP COF.

Table 3 presents a comparative analysis of this work with previously reported materials in two-electrode configurations. The TDMTA-TFP COF synthesized in this study exhibits a moderate specific capacitance of 33.34 F/g at 0.48 A/g, outperforming several earlier COF-based electrodes such as TPT-CTFs (13 F/g), CTF-600 (16 F/g), and TPT@BDA-COF in CH_3COONa (17.8 F/g). Although its capacitance is lower than that of high-performing materials like Co_3S_4@$NiCo_2S_4$ (224.2 F/g) and TpPa-$(OH)_2$/rGO-3 (197.1 F/g), the TDMTA-TFP COF demonstrates exceptional cycling stability, retaining 99.31% of its capacitance after 5,000 cycles—significantly outperforming materials such as the TpOMe-DAQ sheet (65%) and COF/rGO hybrid (70%). Furthermore, it achieves a commendable energy density of 12.20 Wh/kg and a power density of 320.24 W/kg, surpassing several COF-based electrodes including TpOMe-DAQ (2.9 µWh/cm^2) and IITR-COF-1 (17 Wh/kg). Overall, TDMTA-TFP COF offers a well-balanced combination of specific capacitance, energy and power density, and long-term cycling stability, highlighting its potential as a promising candidate for next-generation supercapacitor applications.

Table S3: Comparative analysis of this work with previously reported materials in two-electrode configurations.

Electrode material	**Electrolyte**	**Capacitance**	**Current density/ Scan rate**	**% Retention**	**Energy density**	**Power density**	**Reference(s)**
TPT-CTFs	1 M H_2SO_4	13 F/g	10 A/g	105% after 10000 repetitions	4.2 Wh /kg	250 W /kg	[20]
CTF-600	1MKOH	16F/g	2.50A/g	Almost retained after 10,000 repetitions	8 Wh/kg	250W/ kg	[21]
PDC–MA–COF	6 M KOH aqueous solution	94 F g^{-1}	1.0 A /g	88% of the initial capacitance after 20 000 repetitions	29.2 W h /kg	750 W /kg	[22]
IITR-COF-1	0.5 M K_2SO_4 (aq)	30.5F g^{-1}	0.12 A/g	111.3% retention after 10K cycles	17.0W h kg^{-1}	119.3 W kg−1	[23]
COF/rGO hybrid	1 M.H_2SO_4	74 F g^{-1}	0.1 A g 1	retain 70% of its capacitance at 20 A g-1	10.3 Wh kg−1	50 W Kg^{-1}	[24]
TpOMe-DAQ sheet	2 M aq. H_2SO_4	8.8 F g^{-1} (84 mF cm^{-2})	5 mA cm^{-2}	65% retention of its initial capacitance over 50000 cycles	2.9 µWh cm^{-2}	61.8 µWcm^{-2}	[13]
TFPDQGO-75	1 M NaCl	118.5Fg^{-1}	1A g^{-1}	at 10 A g^{-1}, retained 80.6% its initial capacitance after 10 000 cycles	59.4 Wh kg^{-1}	950 Wkg^{-1}	[10]

TpPa-(OH)$_2$/rGO-3	1 M H_2SO_4	197.1 F/g	0.2 A/g	capacitance retention of about 73.1% for 10,000 cycles	16.6 Wh/kg	158.7 W/kg	[25]
Co_3S_4@$NiCo_2S_4$ (CS/NCZS//CTPC-700-3)	6 M KOH	224.2 F g^{-1}	1 A g^{-1}	retain 79.3% of the initial specific capacitance after 10000 cycles	79.7 Wh kg^{-1}	693.5 W kg^{-1}	[26]
SLD-COFs	3M KOH	41.7 F/g	0.5 A g^{-1}	NA	NA	NA	[27]
TPT@BDA-COF	1M CH_3COONa	17.8 F/g	0.2A/g	NA	17.8 Wh/kg	NA	[28]
TPT@BDA-COF	1M Na_2SO_4	36.9 F/g	0.2A/g	NA	36.9 Wh/kg	NA	[28]
TPT@BDA-COF	1M $NaNO_3$	43.7 F/g	0.2A/g	NA	43.7 Wh/kg	NA	[28]
TPT@BDA-COF	1M $NaClO_4$	47.7 F/g	0.2A/g	105.9% capacitanceretention Afternearly 6000 cycles	47.7 Wh/kg	NA	[28]
TDMTA-TFP-COF	1M KCl	33.34 F/g	0.48 A/g	99.31% after 5,000 cycles	12.20 Wh/kg	320.24 W/kg	**This Work**

Table S4 shows comparison of three-electrode data between the COF material in this study and previously reported materials, focusing on intrinsic electrochemical performance under similar conditions, independent of full device configuration. While comparing our results with previous reports (Table S4), it is found that a COF named as TPT-CTFs developed by Shanxin Xiong et al., exhibited a relatively low specific capacitance of 110 F/g at a current density of 0.1 A/g.[20] In contrast, Xiangjing Zhang et al. demonstrated that high-temperature-modified CTF-600 achieved a significantly higher capacitance of 458 F/g at 0.25 A/g.[29] Similarly, Arijit Maity et al. found that CTF-Py-700 displayed an impressive capacitance of 435 F/g at 1 A/g in the negative potential window,[30] comparable to the 434.03 F/g reported here for TDMTA-TFP-COF a scan rate of 5 mV/s. Meanwhile, Li et al. observed that PDC–MA–COF exhibited a slightly lower capacitance of 335 F/g at 1.0 A/g.[22] Piyali Bhanja et al. also reported a substantial energy-storage capacity for TDFP-1, with a specific capacitance of 354 F/g at a scan rate of 2 mV/s.[31] Among these materials, CTF-600 stands out with the highest capacitance, while our COF (TDMTA-TFP-COF) presented in this study shows comparable performance to CTF-Py-700. (Table S3) Notably, TDMTA-TFP-COF not only demonstrated a high specific capacitance but also excelled in power density. At a current density of 2.86 A/g, it exhibited a specific capacitance of 327.29 F/g and a specific capacity of 748.06 C/g. More importantly, it delivered an outstanding power density of 4228.96 W/kg, while slightly lower than TDFP-1 still surpasses many previously reported materials. Additionally, it achieved a high energy density of 307.56 Wh/kg, making it a promising candidate for high-performance energy storage applications.

- COF/rGO hybrid exhibited a capacitance of 321 F/g at 0.05 A/g with an energy density of 10.3 Wh/kg in 1 M H_2SO_4. While the capacitance is lower than that of TDMTA-TFP COF, the significantly lower energy density indicates superior energy storage capability in the present work.
- $Ti_3C_2TX/ZIF\text{-}67/CoV_2O_6$ delivered a capacitance of 285 F/g at 1 A/g, which is lower than TDMTA-TFP COF, despite using a different electrolyte.
- TpOMe-DAQ sheet achieved a capacitance of 169 F/g at 3.3 mA cm^{-2} in 3 M H_2SO_4, indicating lower charge storage capacity compared to the current material.
- TFPDQGO showed a comparable capacitance of 429 F/g at 2 A/g in 1 M NaCl. However, its energy density of 59.4 Wh/kg is significantly lower than that of TDMTA-TFP COF, suggesting enhanced energy storage performance in this study.
- TpPa-$(OH)_2$/rGO-3 demonstrated a capacitance of 371.1 F/g at 0.5 A/g in 1 M H_2SO_4, which, while notable, is still lower than the capacitance achieved by TDMTA-TFP COF.
- Co_3S_4@$NiCo_2S_4$ exhibited an exceptionally high capacitance of 2697.7 F/g at 1 A/g in 6 M KOH, with an energy density of 79.7 Wh/kg. Although impressive, the use of a strong alkaline electrolyte may limit long-term stability and practical applications compared to the more benign KCl electrolyte used in this work.

SLD-COFs and CoZn@NC materials showed significantly lower capacitance values of 41.7 F/g and 271.14 F/g, respectively, at 0.5 A/g in KOH, further emphasizing the superior performance of TDMTA-TFP COF.

In summary, TDMTA-TFP COF demonstrates an excellent balance of high capacitance and energy density in a milder electrolyte (1 M KCl), making it a highly promising material for supercapacitor applications in three-electrode configurations.

Table S4: Comparison of electrochemical results in a three-electrode configuration for different electrode materials with this work.

Electrode materials	**Electrolyte**	**Capacitance**	**Current density**	**Reference**
TPT-CTFs	1 M H_2SO_4	110 F/g	0.1 A/g	20
CTF-600	1MKOH	458 F/g	0.25A/g	21
CTF-Py-700	1 M Na_2SO_4 aqueous	435 Fg^{-1}	1 A/g	32
PDC–MA–COF	6 M KOH aqueous solution	335 F g^{-1}	1.0 A /g	22
TDFP-1	0.1 M H_2SO_4	418 Fg^{-1}	0.5 Ag^{-1}	31
IITR-COF-1	0.5 M K_2SO_4 (aq)	182.6 F g^{-1}	0.3A/g	23
COF/rGO hybrid	1 M.H_2SO_4	321 F g^{-1}	0.05A/g	24
$Ti_3C_2TX/ZIF\text{-}67/CoV_2O_6$	3.0 M KOH	285 F/g	1A/g	33

TpOMe-DAQ sheet	3 M aq. H_2SO_4	169 F g^{-1}	3.3 mA cm^{-2}	13
TFPDQGO	1 M NaCl	429.0 F g^{-1}	2A g^{-1}	10
$TpPa-(OH)_2$	1 M H_2SO_4	103.4 F g^{-1}	0.5 A/g	25
$TpPa-(OH)_2$/rGO-3	1 M H_2SO_4	371.1F/g	0.5 A/g	25
Co_3S_4@$NiCo_2S_4$ (CS/NCZS)	6 M KOH	2697.7 F g^{-1}	1 A g^{-1}	26
CoZn@NC	1M KOH	271.14 F/g	0.5 A g-1	34
TPT-DAHQ COF	1M KOH	256 F/g	0.5 A/g	35
TPTP-COF	6M KOH	56.4 F/g	5.0 mV s $^{-1}$	36
TPDA-COF	6M KOH	70.6 F /g	5.0 mV s $^{-1}$	36
TDMTA-TFP-COF	1M KCl	434.03 F/g	2.86 A/g (5 mV/s)	**This Work**

Table S5: Coulombic efficiency measured at different current densities for symmetric supercapacitor

Current Density	**CE**
0.95	74.4
1.43	86.2
1.90	90.45
2.38	93.61
3.81	95.10

One limitation of the TDMTA-TFP COF is that purely organic frameworks typically exhibit lower capacitance compared to metal-containing materials, such as metal oxides, metal sulfides, and metal-organic frameworks (MOFs), due to the absence of highly redox-active metal centers.

Another class of reticular materials is Metal–organic frameworks (MOFs), which are extensively researched as supercapacitor electrode materials because they often display superior conductivity, higher specific capacitance, and greater energy and power density. However, MOFs usually have poor stability in the required electrolytic medium due to weak coordination interactions between metal ions and ligands, which results in a shorter cycle life in electrochemical tests. On the other hand, because of their strong covalent bonding, COFs have improved electrochemical stability [22]The incorporation of metal ions or clusters into COF structures could enhance charge storage through additional faradaic reactions, thereby boosting capacitance and energy density. In future studies, metal-doped COFs or metal-covalent organic frameworks (MCOFs) could be explored as promising materials for supercapacitor devices, combining the structural benefits of COFs with the enhanced electrochemical performance provided by metal species.

References:

1. N. Troullier and J. L. Martins, *Physical Review B*, 1991, **43**, 1993-2006.
2. J. Junquera, Ó. Paz, D. Sánchez-Portal and E. Artacho, *Physical Review B*, 2001, **64**, 235111.
3. J. P. Perdew, K. Burke and M. Ernzerhof, *Physical Review Letters*, 1996, **77**, 3865-3868.

4. Y. Kashyap, P. R, R. R. Pandey, A. Andola, D. H. Nagaraju and R. K. Pandey, *Journal of Solid State Electrochemistry*, 2024, **28**, 3357-3365.
5. J. Chen, C. Jiang, Z. Xing, J. Li, F. Dai and Y. Peng, *New Journal of Chemistry*, 2023, **47**, 6759-6764.
6. S. Kandambeth, A. Mallick, B. Lukose, M. V. Mane, T. Heine and R. Banerjee, *J. Am. Chem. Soc.*, 2012, **134**, 19524-19527.
7. H. Bhambri, S. Khullar, Sakshi and S. K. Mandal, *Materials Advances*, 2022, **3**, 19-124.
8. X. Zhao, P. Pachfule, S. Li, T. Langenhahn, M. Ye, C. Schlesiger, S. Praetz, J. Schmidt and A. Thomas, *J. Am. Chem. Soc.*, 2019, **141**, 6623-6630.
9. S. Bhunia, S. K. Das, R. Jana, S. C. Peter, S. Bhattacharya, M. Addicoat, A. Bhaumik and A. Pradhan, *ACS Applied Materials & Interfaces*, 2017, **9**, 23843-23851.
10. L. Xu, Y. Liu, Z. Ding, X. Xu, X. Liu, Z. Gong, J. Li, T. Lu and L. Pan, *Small*, 2024, **20**, 2307843.
11. S. Kandambeth, J. Jia, H. Wu, V. S. Kale, P. T. Parvatkar, J. Czaban-Jóźwiak, S. Zhou, X. Xu, Z. O. Ameur, E. Abou-Hamad, A.-H. Emwas, O. Shekhah, H. N. Alshareef and M. Eddaoudi, *Advanced Energy Materials*, 2020, **10**, 2001673.
12. R. R. Pandey, Y. Kashyap, A. Andola, H. Nakanishi and R. K. Pandey, *ChemistrySelect*, 2023, **8**, e202302042.
13. A. Halder, M. Ghosh, A. Khayum M, S. Bera, M. Addicoat, H. S. Sasmal, S. Karak, S. Kurungot and R. Banerjee, *J. Am. Chem. Soc.*, 2018, **140**, 10941-10945.
14. L. Wang, X. Feng, L. Ren, Q. Piao, J. Zhong, Y. Wang, H. Li, Y. Chen and B. Wang, *J. Am. Chem. Soc.*, 2015, **137**, 4920-4923.
15. N. Singh, D. Yadav, S. V. Mulay, J. Y. Kim, N.-J. Park and J.-O. Baeg, *ACS Applied Materials & Interfaces*, 2021, **13**, 14122-14131.
16. P. Makuła, M. Pacia and W. Macyk, *The Journal of Physical Chemistry Letters*, 2018, **9**, 6814-6817.
17. A. D. D. Wonanke and M. A. Addicoat, *Physical Chemistry Chemical Physics*, 2022, **24**, 15494-15501.
18. C. Winkler and E. Zojer, *arXiv preprint arXiv:2102.08070*, 2021.
19. J. Wang, J. Polleux, J. Lim and B. Dunn, *The Journal of Physical Chemistry C*, 2007, **111**, 14925-14931.
20. S. Xiong, J. Guo, F. Lv, X. Zhao, W. Zhang, X. Wang, C. Hua, R. Zhang, J. Chu, C. Wang, M. Gong and B. Wu, *Journal of Applied Polymer Science*, 2023, **140**, e54538.
21. X. Zhang, Z. Zhang, R. Xiong, X. Xu, X. Tian and C. Wang, *Chemistry Letters*, 2022, **51**, 854-858.
22. L. Li, F. Lu, R. Xue, B. Ma, Q. Li, N. Wu, H. Liu, W. Yao, H. Guo and W. Yang, *ACS Applied Materials & Interfaces*, 2019, **11**, 26355-26363.
23. Y. Kumar, I. Ahmad, A. Rawat, R. K. Pandey, P. Mohanty and R. Pandey, *ACS Applied Materials & Interfaces*, 2024, **16**, 11605-11616.
24. C. Wang, F. Liu, J. Chen, Z. Yuan, C. Liu, X. Zhang, M. Xu, L. Wei and Y. Chen, *Energy Storage Materials*, 2020, **32**, 448-457.
25. D. Hu, Y. Jia, S. Yang, C. Lin, F. Huang, R. Wu, S. Guo, K. Xie and P. Du, *Chemical Engineering Journal*, 2024, **488**, 151160.
26. C. Ni, X. Wang, X. Cai, C. Yu, Q. Wu, Y. Shen and C. Hao, *Journal of Materials Science & Technology*, 2025, **210**, 233-245.
27. J. Yang, H. You, Y. Han, H. Chen, K. Zhang, Y. Li, J. Bao, X. Ge, G. Pan and R. Xing, *ACS Applied Materials & Interfaces*, 2025, **17**, 11027-11035.
28. I. Ahmad, O. Singh, J. Ahmed, Priyanka, S. M. Alshehri, C. Bharti and Vidivay, *Chemistry – An Asian Journal*, 2025, **20**, e202401149.
29. J. Li, X. Jing, Q. Li, S. Li, X. Gao, X. Feng and B. Wang, *Chemical Society Reviews*, 2020, **49**, 3565-3604.
30. A. Maity, M. Siebels, A. Jana, M. Eswaran, R. Dhanusuraman, C. Janiak and A. Bhunia, *ChemSusChem*, 2025, **18**, e202401716.

31. P. Bhanja, K. Bhunia, S. K. Das, D. Pradhan, R. Kimura, Y. Hijikata, S. Irle and A. Bhaumik, *ChemSusChem*, 2017, **10**, 921-929.
32. A. Maity, M. Siebels, A. Jana, M. Eswaran, R. Dhanusuraman, C. Janiak and A. Bhunia, *ChemSusChem*, 2024, **n/a**, e202401716.
33. C. Liu, Y. Bai, W. Li, F. Yang, G. Zhang and H. Pang, *Angewandte Chemie International Edition*, 2022, **61**, e202116282.
34. M. S. Esmaeili, M. Mehrpooya and M. R. Ganjali, *International Journal of Hydrogen Energy*, 2025, **97**, 483-500.
35. A. F. M. El-Mahdy, Y.-H. Hung, T. H. Mansoure, H.-H. Yu, T. Chen and S.-W. Kuo, *Chemistry – An Asian Journal*, 2019, **14**, 1429-1435.
36. H.-C. Yang, Y.-Y. Chen, S.-Y. Suen and R.-H. Lee, *Polymer*, 2023, **273**, 125853.